Materials & Design 225 (2023) 111428

Contents lists available at ScienceDirect

Materials & Design

journal homepage: www.elsevier.com/locate/matdes

A novel approach to fabricate load-bearing Ti6Al4V-Barium titanate piezoelectric bone scaffolds by coupling electron beam melting and field-assisted sintering

Abdullah Riaz [a,*,1], Christian Polley [a,1], Henrik Lund [b], Armin Springer [c], Hermann Seitz [a,d]

[a] University of Rostock, Microfluidics, Faculty of Mechanical Engineering and Marine Technology, Justus-von-Liebig-Weg 6, 18059 Rostock, Germany
[b] Leibniz Institute for Catalysis, Albert-Einstein-Straße 29a, 18059 Rostock, Germany
[c] University Medical Center Rostock, Medical Biology and Electron Microscopy Centre, Strempel-Str. 14, 18057 Rostock, Germany
[d] University of Rostock, Department of Life, Light and Matter, Albert Einstein-Str. 25, 18059 Rostock, Germany

HIGHLIGHTS

- Electron beam melting and field-assisted sintering were coupled to fabricate load-bearing Ti6Al4V-$BaTiO_3$ piezoelectric bone scaffolds.
- Images of sintered composite scaffold interface revealed that the Ti6Al4V cylindrical lattice structure bounded with $BaTiO_3$ matrix without its major deformation.
- The fabricated Ti6Al4V-$BaTiO_3$ scaffold showed a piezoelectric response of (0.63 ± 0.12) pC/N without poling which increased to (4.92 ± 0.75) pC/N after corona poling.
- Nanoindentation values reveal that Ti6Al4V is the harder and stiffer part of the Ti6Al4V-$BaTiO_3$ scaffold.

GRAPHICAL ABSTRACT

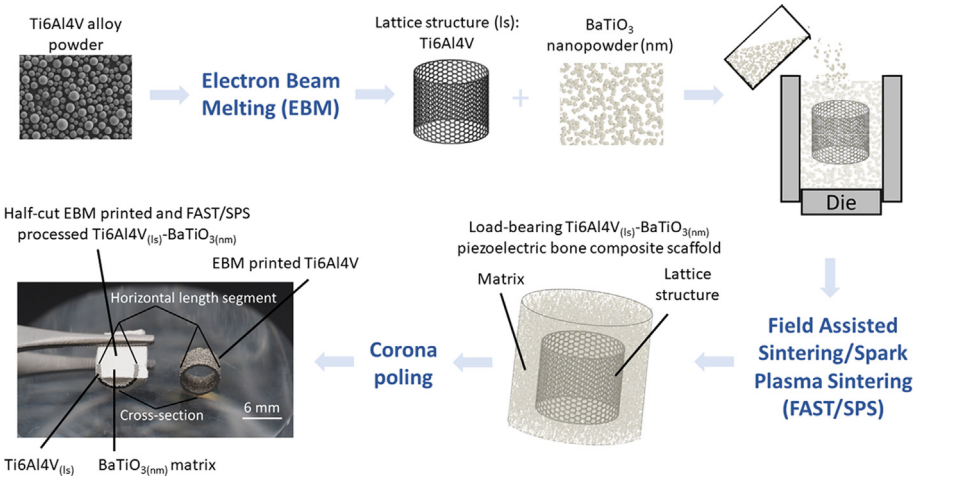

ARTICLE INFO

Article history:
Received 20 October 2022
Revised 22 November 2022
Accepted 23 November 2022
Available online 24 November 2022

Keywords:
Electron beam melting
Field-assisted sintering
Load-bearing scaffold
Corona poling
Metal-ceramic composite
Piezoelectric effect

ABSTRACT

A critical-size bone defect in load-bearing areas is a challenging clinical problem in orthopaedic surgery. Titanium alloy (Ti6Al4V) scaffolds have advantages because of their biomechanical stability but lack electrical activity, which hinders their further use. This work is focused on the fabrication of Ti6Al4V-Barium Titanate ($BaTiO_3$) bulk composite scaffolds to combine the biomechanical stability of Ti6Al4V with electrical activity through $BaTiO_3$. For the first time, a hollow cylindrical Ti6Al4V is additively manufactured by electron beam melting and combined with piezoelectric $BaTiO_3$ powder for joint processing in field-assisted sintering. Scanning electron microscope images on the interface of the Ti6Al4V-$BaTiO_3$ composite scaffold showed that after sintering, the Ti6Al4V lattice structure bounded with $BaTiO_3$ matrix without its major deformation. The Ti6Al4V-$BaTiO_3$ scaffold had average piezoelectric constants of (0.63 ± 0.12) pC/N directly after sintering due to partial dipole alignment of the $BaTiO_3$ tetragonal phase, which increased to (4.92 ± 0.75) pC/N after a successful corona poling. Moreover, the nanoindentation values of Ti6Al4V exhibited an average hardness and Young's modulus of (5.9 ± 0.9) GPa and (130 ± 14) GPa,

* Corresponding author.
E-mail address: abdullah.riaz@uni-rostock.de (A. Riaz).
[1] Authors contribute equally.

https://doi.org/10.1016/j.matdes.2022.111428

and $BaTiO_3$ showed (4.0 ± 0.6) GPa and (106 ± 10) GPa, respectively. It reveals that the Ti6Al4V is the harder and stiffer part in the Ti6Al4V-$BaTiO_3$ composite scaffold. Such a scaffold has the potential to treat critical-size bone defects in load-bearing areas and guide tissue regeneration by physical stimulation.

1. Introduction

Bone is a highly vascularised tissue that is subject to permanent remodelling processes [1]. This property enables bone to heal defects quickly and effectively. However, if these defects reach critical sizes, for example, because of trauma or tumour resection, this exceeds the self-regenerative properties of the bone, and the defect must be filled accordingly in order to achieve convalescence [2]. Today, autologous or allogeneic bone replacement continues to represent the gold standard, with up to 2.2 million procedures worldwide annually [2,3]. Even though the outcome of transplantation is usually good, there are still risks, e.g. limited availability of healthy donor tissue, creation of a second defect and infection [2]. Therefore, there is still a need for synthetic biomaterials (scaffolds) that can satisfactorily fill bone defects, have mechanical properties like bone, and provide sufficient osteointegration and biocompatibility.

In particular, the use of inert titanium alloys such as Ti6Al4V has proven to be advantageous for use as implants, especially in load-bearing areas, due to their high mechanical strength, resistance to fracture and fatigue properties. However, titanium alloys represent phase one biomaterials and lack properties such as bioactivity or the ability to actively stimulate tissue regeneration [4]. In recent years, several publications have shown that electrically active ceramic and polymer biomaterials can take over these functions [5,6]. They mimic the piezoelectric properties of bone and are thus able to promote bone healing [6–8].

In particular, the piezoelectric effect of the piezoelectric scaffold can be used as an energy conversion source that converts the mechanical stress generated when patient walks into electrical signals to electrically stimulate bone cells [7]. The biomimetic microenvironment created by the piezoelectric scaffold triggers bone growth in the critical size bone defect due to electromechanical stimulation [9,10]. This stimulation can lead to rapid bone regeneration and complete mature bone-structure formation integrated with intact natural bone. In general, the Human Mesenchymal Stem Cells (HMSCs) can be induced to differentiate into osteoblasts by the piezoelectric scaffold as described in Fig. 1 [11,12]. For instance, it has been reported by many authors that Barium Titanate ($BaTiO_3$) is a promising candidate for biocompatible piezoelectric ceramic scaffolds [13–15]. Its piezoelectric properties can be combined with Ti6Al4V scaffolds to develop a composite material that can potentially fill bone defects particularly in load-bearing areas.

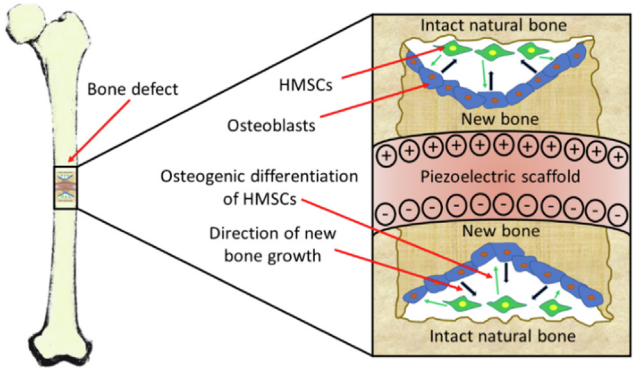

Fig. 1. Illustration of biomimetic microenvironment created by piezoelectric scaffold encouraging critical size bone defect repair. Human Mesenchymal Stem Cells (HMSCs) can be induced to differentiate into osteoblasts and the piezoelectric scaffold can give rise to rapid bone regeneration and complete mature bone-structure formation integrated with intact natural bone [10].

In recent years, researchers have been utilising an Additive Manufacturing (AM) approach to fabricating scaffold parts layer by layer, as an alternative to subtractive manufacturing methodologies. For instance, Electron Beam Melting (EBM) as an AM technique is suitable for manufacturing metallic scaffolds for bone tissue engineering in load-bearing areas [16,17]. To make the EBM printed titanium alloy scaffolds electrically active, a coating with piezoelectric ceramics have been reported [13–15]. The studies showed improved osteogenesis and osteointegration on piezoelectric coated scaffolds. The piezoelectric constant (d_{33}) values of coated scaffold and the macroscopic analysis with piezoelectric characterisation are hardly discussed. Nevertheless, the reported microscopic d_{33} value (0.7 pC/N) of coated scaffold is relatively smaller than the standard piezoelectric constants of biocompatible scaffolds even after poling treatment [8,14,18,19]. This piezoelectric constant strength could most probably be increased if the composite scaffold such as bulk metal-ceramic composite scaffold is fabricated. However, the synthesis of bulk multi-materials, especially metal-ceramics composite, and their sintering, is still challenging.

Field-Assisted Sintering Technique/Spark Plasma Sintering (FAST/SPS) could be a promising way to achieve improved mechanical and scaffold-bone tissue interface properties [20]. FAST/SPS is an advanced sintering process that uses pulsed direct current and pressure to assist densification and allows the sintering of multi-materials and composites. It is an alternative to conventional casting in the synthesis of high-performance medical scaffolds such as metals, ceramics, or their composites. The combination of two manufacturing techniques, such as EBM and FAST/SPS, may enable the fabrication of metal-ceramic composites, which can be suitable for electrically active load-bearing implant applications. However, the processing of EBM printed metal complex parts together with ceramic powder is a challenging task. The combination of applied mechanical stress in FAST/SPS with relatively high sintering temperatures required to sinter ceramics compared to metals can cause major deformation of the metal printed part [20,21]. In addition, post-processing such as polarisation of piezoelectric ceramic that contains metal alloy inside, is yet another challenge. These might be the major reasons for no existing research paper on EBM printing of titanium alloys and its combination with FAST/SPS to fabricate metal-ceramic piezoelectric composite scaffolds. The unconventional approach in FAST/SPS can help sintering complex shapes which include FAST/SPS tools design, using sacrificial material, pressureless and cold FAST/SPS process [21–23]. Therefore, the limitation of the complex shape of the EBM printed part and process parameters of EBM and FAST/SPS must be carefully chosen.

The studies focused on bone scaffolds for load-bearing areas have either used titanium alloys without piezoelectric biomaterials or only coating with the piezoelectric ceramics [13–15,24–26]. However, bulk metal-ceramic composite scaffolds with piezoelec-

tric properties for load-bearing areas is not considered, which is the aim of this study. For the first time, Ti6Al4V is fabricated by EBM and combined with piezoelectric $BaTiO_3$ powder for joint processing in FAST/SPS and afterwards polarised through corona poling. Moreover, Scanning Electron Microscopy (SEM) and Energy-Dispersive X-ray (EDX) spectroscopy are used to analyse the surfaces and interfaces of both materials. The crystal structure, mechanical and piezoelectric properties of the composite scaffold are assessed by X-Ray Diffraction (XRD), and nanoindentation and piezoelectric measurements, respectively.

2. Materials and fabrication methods

2.1. Materials

Ti6Al4V-ELI (grade 23) alloy powder supplied by Arcam SE was used for EBM printing and later for the processing of the EBM printed lattice structure ($Ti6Al4V_{(ls)}$) in FAST/SPS together with piezoelectric $BaTiO_3$ powder. Moreover, the commercially available $BaTiO_3$ powders from Sigma-Aldrich/Merck KGaA, Darmstadt, Germany, were used for FAST/SPS densification process. Two different particle sizes of piezoelectric $BaTiO_3$; nanopowder ($BaTiO_{3(nm)}$) with the particle size of ~50 nm and < 3 μm size powder ($BaTiO_{3(\mu m)}$) were selected. These two different particle sizes of $BaTiO_3$ power were used to study their influence on the densification process during sintering and to check their suitability for join processing in FAST/SPS together with EBM printed $Ti6Al4V_{(ls)}$.

2.2. Coupling of electron beam melting and field-assisted sintering

A Hollow cylindrical scaffold with a hexagonal honeycomb structure (d = 6 mm, h = 4 mm) and a pore size of 400 μm was designed and merged with the CAD software Netfabb Premium 2019 (Autodesk, San Rafael, USA). Build job preparation and scaling were performed with Magics 2016 (Materialise, Leuven, Belgium). The samples were sliced in 50 μm layers using Arcam's proprietary software and built on an A1 machine (Arcam SE/ GE Additive, Mölndal, Sweden). To remove residual powder the powder recovery system from Arcam was used.

To sinter the samples, the HP D5 FAST/SPS unit (FCT Systeme GmbH, Rauenstein, Germany) located in the FAST laboratory, University of Rostock, Germany, was utilised. The samples were filled into the graphite die one after another and sintered. Protective graphite foil was also placed between the powder and inner walls of the die and the punches.

Initially, pure $BaTiO_{3(nm)}$ and $BaTiO_{3(\mu m)}$ (without $Ti6Al4V_{(ls)}$) were sintered and examined successively at different sintering temperatures and pressures. Afterwards, the EBM printed $Ti6Al4V_{(ls)}$ was introduced into the die in a cross-sectional direction (see graphical abstract) and $BaTiO_{3(nm)}$ was subsequently added to fill in the die and sintered. In preliminary sintering processes for the fabrication of $Ti6Al4V_{(ls)}$-$BaTiO_{3(nm)}$ composite, the sintering temperature and applied load were varied to find the best sintering conditions to ensure the maximum densification of $BaTiO_3$ powder and avoid damaging the shape of the hollow cylindrical $Ti6Al4V_{(ls)}$ scaffolds. The temperature varied from 950 °C to 1050 °C and the applied load varied from 3 kN to 6 kN, resulting in a pressure of approximately 36 MPa to 76 MPa inside the die. As the temperature increased, the densification of $BaTiO_3$ also increased but this also resulted in the destruction of the $Ti6Al4V_{(ls)}$. However, an increase in pressure to 76 MPa as cold pressing did not destroy the $Ti6Al4V_{(ls)}$. Motivated by this, a sintering temperature of 950 °C and pressure of 76 MPa were selected to achieve maximum possible densification and to avoid the destruction of $Ti6Al4V_{(ls)}$. The samples were sintered for 5 min at an elevated temperature and in a vacuum of approximately 1 mbar and then cooled down with a natural cooling rate of approximately 200 K/min between 950 °C and 400 °C and then about 50 K/min to room temperature. To control the heating processes above 400 °C, an optical pyrometer was focused in a hole drilled in the upper part of a graphite punch and when below 400 °C this was monitored by a thermocouple which was attached to the graphite die. During the sintering process, the position and movement of the plunger were also measured with a capacitive sensor which was mechanically coupled to the upper punch and served as a probe to monitor the densification of the powder.

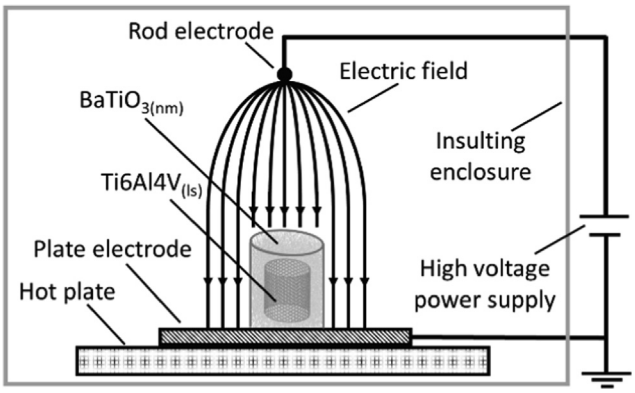

Fig. 2. Schematic diagram of setup for corona poling.

The diameters of the samples after sintering were ~10 mm with different heights of ~8-12 mm. To adjust the height of the $Ti6Al4V_{(ls)}$-$BaTiO_{3(nm)}$ composite for further experiments following the corona poling and piezoelectric measurements, the samples were precisely cut in cross-section and horizontal length segments using a diamond band saw. Lastly, the sample was embedded in a resin and polished using ATM Brillant (Mammelzen, Germany).

2.3. Corona poling

An in-house corona poling setup as shown in Fig. 2 was used to polarise the FAST/SPS processed $Ti6Al4V_{(ls)}$-$BaTiO_{3(nm)}$ composite scaffold. The setup consists of two opposing copper electrodes, one of which was a rod electrode and the other was a plate electrode. Both electrodes were connected to a high voltage power supply (HNCs 10000–180 pos., Heinzinger, Rosenheim, Germany) and were connected to the ground. Before the polarisation process, the samples were pre-heated to 140 °C for 15 min in a furnace. The heated samples were polarised during their cooling phase in the corona poling setup with an electric field strength of 1.2 kV/mm for 15 min. These poling parameters were chosen based on the results obtained in the previous study [8].

3. Experiments

3.1. Density measurements

The average densities (ρ_{avg}) of five measurements of the samples were determined using the gas pycnometer Ultrapyc 5000 Foam from Anton Paar (Graz, Austria). It is a fully automated benchtop helium pycnometer for high-precision, non-destructive determination of solid density in accordance with international standards.

3.2. Scanning electron microscopy and energy-dispersive X-ray spectroscopy

Sample images were analysed by a field emission Scanning Electron Microscope (SEM, MERLIN® VP Compact, Co. Zeiss,

Oberkochen) equipped with an EDX detector (XFlash 6/30, Co. Bruker, Berlin). A representative area of the samples was also analysed and mapped for elemental distribution on the basis of the EDX-spectra data by QUANTAX ESPRIT Microanalysis software (version 2.0). Prior to the measurements, the resin-embedded sample was coated with carbon (4.0 nm thickness; CCU-010, Co. safematic GmbH, Zizers, Switzerland) and mounted directly on the sample carrier with conductive carbon tape (Co. PLANO, Wetzlar, Germany).

3.3. X-ray diffraction

XRD patterns of powder $BaTiO_{3(nm)}$ and FAST/SPS processed $Ti6Al4V_{(ls)}$-$BaTiO_{3(nm)}$ composite were recorded on a Panalytical X'Pert θ/2θ -diffractometer equipped with Xcelerator detector using automatic divergence slits and Cu $k\alpha_1/\alpha_2$ radiation (40 kV, 40 mA; λ = 0.15406 nm, 0.154443 nm). Cu beta-radiation was excluded using a nickel filter foil. The measurements were performed with $0.021°s^{-1}$ or $0.011°s^{-1}$, respectively. The $BaTiO_3$ powder was mounted on silicon zero background holders and the sintered $Ti6Al4V_{(ls)}$-$BaTiO_{3(nm)}$ composite scaffold was mounted on modelling clay and manually adjusted to correct the sample height. Obtained intensities were converted from automatic to fixed divergence slits (0.25°) for further analysis. Peak positions and profiles were fitted with the Pseudo-Voigt function using the HighScore Plus software package (Panalytical). Phase identification was done by using the PDF-2 database of the International Center of Diffraction Data (ICDD) and crystallite sizes were calculated by applying the Scherrer equation using the integral breadth under the assumption of spherically shaped crystallites.

3.4. Piezoelectric measurement

The direct piezoelectric effect of the $Ti6Al4V_{(ls)}$-$BaTiO_{3(nm)}$ composite scaffold was investigated with the Berlincourt method using a d_{33} piezometer (PM300, PIEZOTEST, Singapore). The samples were clamped between two flat electrodes with a force of 10 N. Afterwards, an oscillating force of 0.2 N with a frequency of 110 Hz was applied, and piezoelectric constant (d_{33}) value was observed. The positive and negative piezoelectric constants (d_{33+} and d_{33-}) were measured both before and after polarisation of sintered sample with corona poling. Each of the data points was averaged from three measurements.

3.5. Nanoindentation tests

Nanoindentation tests were carried out on the FAST/SPS processed $Ti6Al4V_{(ls)}$-$BaTiO_{3(nm)}$ composite scaffold using a calibrated nanoindentation CERT UMT multi-specimen test system equipped with a standard Berkovich indenter from Bruker NANO GmbH (Karlsruhe, Germany). To measure the hardness and Young's modulus, the Oliver-Pharr method was implemented [27]. First, the tests were performed on the cross-sectional surface of the Ti6Al4V region of the sample by applying the step-by-step forces of 10, 25, 50, 75, 100, 200, 300 and 400 mN to drive an indenter into the surface of the sample during the loading process and then unloaded after achieving each of the peak loads. The measurements were subsequently repeated to carry out identical tests on the cross-sectional surface of the $BaTiO_3$ region of the sample. Each of the data points was averaged from five tests. The peak loads and indenter displacements into the samples were then observed and the hardness and Young's modulus were estimated using a UMT Test Viewer, CETR Inc. software.

4. Results and discussion

4.1. Densification behaviour

The densification behaviour of $BaTiO_{3(nm)}$, $BaTiO_{3(\mu m)}$ and $Ti6Al4V_{(ls)}$-$BaTiO_{3(nm)}$ composite scaffold over the process temperature and at a constant pressure of 76 MPa is presented in Fig. 3. A similar trend in the plunger displacement is noticed during the sintering of $BaTiO_{3(nm)}$ and $Ti6Al4V_{(ls)}$-$BaTiO_{3(nm)}$. In contrast, the displacement is quite different for the sintering of $BaTiO_{3(\mu m)}$. The first arrow indicates the Relative Piston Position (RPP) at the start of the temperature monitored by the pyrometer. The second arrow shows the temperature at which the plunger displacement starts indicating the start of the sintering process. Arrow three reveals that the temperature reaches 950 °C which is the starting point of the holding temperature. Following arrow four, which is the end of the holding temperature and the start of the cooling, arrow five shows the end of the cooling process.

When the pressure was applied at the beginning of the process, the plunger displacement occurred and the RPP of $BaTiO_{3(nm)}$ and $Ti6Al4V_{(ls)}$-$BaTiO_{3(nm)}$ reached ~3.5 mm, but $BaTiO_{3(\mu m)}$ was at ~1.9 mm. These RPP indicate that the $BaTiO_{3(nm)}$ is better compressed than $BaTiO_{3(\mu m)}$ before the start of the sintering process

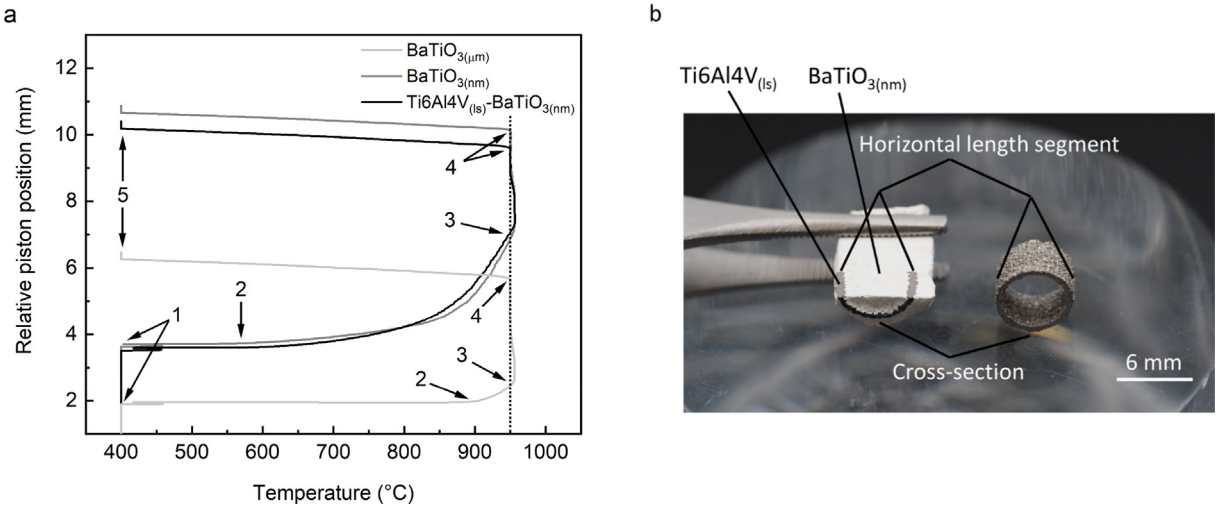

Fig. 3. (a) Plunger displacement as a function of process temperature during the sintering of $BaTiO_{3(\mu m)}$ and $BaTiO_{3(nm)}$, as well as $Ti6Al4V_{(ls)}$-$BaTiO_{3(nm)}$ composite. (b) Original images of a half-cut EBM printed $Ti6Al4V_{(ls)}$ sintered with piezoelectric $BaTiO_{3(nm)}$ matrix (left) along with their corresponding EBM printed $Ti6Al4V_{(ls)}$ (right).

which begins around the temperature of ~575 °C for $BaTiO_{3(nm)}$ and $Ti6Al4V_{(ls)}$-$BaTiO_{3(nm)}$. This temperature range is much lower than $BaTiO_{3(\mu m)}$ which is ~900 °C as well as conventional sintering processes or even by common FAST/SPS process [28,29]. The better compression in the early stage and at the start of sintering at a relatively lower temperature could be due to plastic deformation of nanoparticles, grain rotation, or sliding, assisted by the softening of the particle surfaces [20]. These processes lead to fast densification with limited grain growth.

In addition, the plunger displacement from the start of the sintering temperature (second arrow) to 950 °C (third arrow) associated with $BaTiO_{3(\mu m)}$ displaced only ~0.4 mm indicating that 950 °C is insufficient for the densification of this powder. In contrast, the plunger displacements of $BaTiO_{3(nm)}$ and $Ti6Al4V_{(ls)}$-$BaTiO_{3(nm)}$ are ~3.1 mm and ~3.4 mm, respectively. This significant plunger displacement at a relatively low sintering temperature was found to be suitable for sintering EBM printed $Ti6Al4V_{(ls)}$ together with $BaTiO_{3(nm)}$ powder. Additionally, the slight increase in the displacement of $Ti6Al4V_{(ls)}$-$BaTiO_{3(nm)}$ compared to $BaTiO_{3(nm)}$ is probably promoted by the $Ti6Al4V_{(ls)}$ leading to further densification, since Ti6Al4V alloy can usually be highly densified at around 950 °C [30,31]. The change in RPP continued for all samples during the holding time showing that the sintering continues until the end of the holding time. The achieved relative density of sintered $BaTiO_{3(nm)}$ from $Ti6Al4V_{(ls)}$-$BaTiO_{3(nm)}$ was a little higher than pure $BaTiO_{3(nm)}$ (with $Ti6Al4V_{(ls)}$) as shown in Table 1. This value is close to the values reported in the literature [32]. However, $BaTiO_{3(\mu m)}$ was a mixture of loose and compressed powder. The determined relative density of the EBM printed $Ti6Al4V_{(ls)}$ as well as its dimensions before and after FAST/SPS process are also presented in Table 1. Additionally, to compare the total change in the RPP of $Ti6Al4V_{(ls)}$-$BaTiO_{3(nm)}$ in reference to $BaTiO_{3(nm)}$ and $BaTiO_{3(\mu m)}$, the difference of $Ti6Al4V_{(ls)}$-$BaTiO_{3(nm)}$ was estimated which is just ~4.3 % from $BaTiO_{3(nm)}$ though $BaTiO_{3(\mu m)}$ has a much higher difference of ~38.6 %. This difference in RPP and the post-sintered condition of $BaTiO_{3(\mu m)}$ indicates that it needs a relatively higher temperature for densification. Therefore, $BaTiO_{3(\mu m)}$ is not suitable for its joint sintering process with EBM printed $Ti6Al4V_{(ls)}$. $BaTiO_{3(nm)}$ is, however, far better and workable with $Ti6Al4V_{(ls)}$. Therefore, only $Ti6Al4V_{(ls)}$-$BaTiO_{3(nm)}$ composite scaffold is considered for further study. To visualise this composite scaffold, the image of a half-cut composite scaffold along with its corresponding EBM printed $Ti6Al4V_{(ls)}$ is shown in Fig. 3.

4.2. Scanning electron microscopy and energy-dispersive X-ray spectroscopy

The EBM printed $Ti6Al4V_{(ls)}$ in the horizontal length segment is examined by SEM and presented in Fig. 4a. The pore size of the scaffold is very small according to the set CAD specifications, which is why the small pores were not completely represented. The

Table 1
Determined relative densities and dimensions of the EBM printed and FAST/SPS processed samples.

Samples	Relative density (%)	Inner diameter (mm)	Height (mm)
EBM printed $Ti6Al4V_{(ls)}$, before FAST/SPS	92.6 ± 0.2	~5.27	~4.07
EBM printed $Ti6Al4V_{(ls)}$, after FAST/SPS	–	~5.11	~3.07
$BaTiO_{3(\mu m)}$	–	~10.0	~12.00
$BaTiO_{3(nm)}$	90.1 ± 0.5	~10.0	~7.90
$BaTiO_{3(nm)}$ of $Ti6Al4V_{(ls)}$-$BaTiO_{3(nm)}$	92.0 ± 0.7	~10.0	~8.00

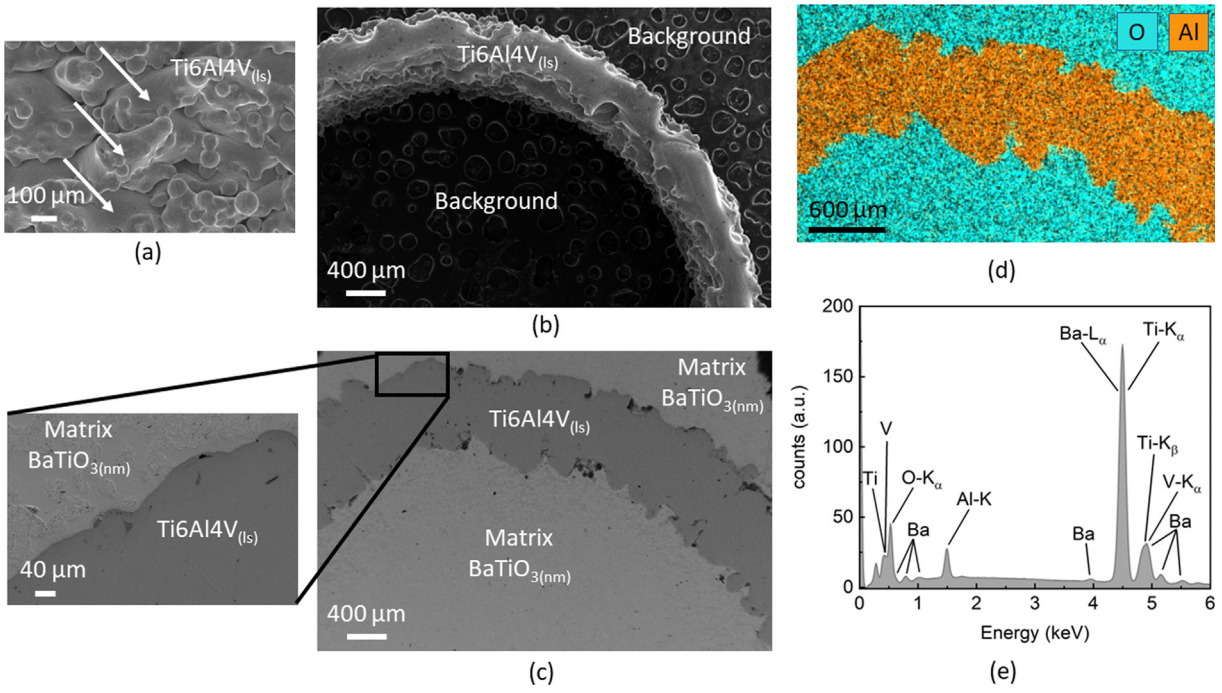

Fig. 4. Exemplary scanning electron microscope images of samples and energy-dispersive X-ray spectrum with elemental mapping. EBM printed $Ti6Al4V_{(ls)}$ before FAST/SPS process (a) in a horizontal length segment and (b) in cross-sectional view. (c) Cross-sectional interface of the FAST/SPS processed $Ti6Al4V_{(ls)}$-$BaTiO_{3(nm)}$ composite with a magnifying view. (d) Cross-sectional elemental mapping of oxygen and aluminium of FAST/SPS processed $Ti6Al4V_{(ls)}$-$BaTiO_{3(nm)}$ composite. (e) The spectrum of the FAST/SPS processed $Ti6Al4V_{(ls)}$-$BaTiO_{3(nm)}$ composite.

arrows show that the walls of the hexagonal honeycomb structure joined each other, this was most likely due to the excess melting and overheating during the EBM printing process. However, the traces of the hexagonal honeycomb structure shape are still present. The top-side view of EBM printed Ti6Al4V$_{(ls)}$ before the FAST/SPS process is also shown in Fig. 4b. The cross-sectional thickness of its lattice structure was estimated to be ~0.74 mm, which is comparable to its counterpart with a slight change in thickness to ~0.86 mm after the FAST/SPS process with $BaTiO_3$ nano-powder as shown in Fig. 4c. This increase in cross-sectional thickness of ~14 % is due to the slight deformation of Ti6Al4V$_{(ls)}$ under applied pressure during sintering at an elevated temperature. Similarly, a maximum height shrinkage of ~25 % was observed in horizontal length segment. The densification of Ti6Al4V$_{(ls)}$ during the FAST/SPS process could have slightly influenced that shrinkage effect together with applied pressure. It could be interpreted that by coupling EBM and FAST/SPS, for instance as presented in this work, a maximum deformation of ~14 % and ~25 % in EBM printed Ti6Al4V$_{(ls)}$ after the FAST/SPS process should be considered in cross-sectional and horizontal length segment, respectively.

Nevertheless, the composite scaffold was successfully fabricated by coupling EBM and FAST/SPS without destroying the shape of EBM fabricated cylindrical lattice structure. In general, a clear deformation is expected to occur during the FAST/SPS process under pressure of complex shapes, especially when ceramics are processed since they require high temperatures for densification [21,22,33]. In contrast, it is clear from the SEM images that the ring-like lattice structure retained its shape during the FAST/SPS process. Additionally, the EBM printed Ti6Al4V$_{(ls)}$ bounded with $BaTiO_{3(nm)}$ without any substantial pores, as shown in Fig. 4c, which are preferentially located at the interface between the lattice structure and matrix [22,34]. However, it is important to mention that in preliminary sintering processes, the major deformation was clearly observed when the applied pressure was in the horizontal length segment of Ti6Al4V$_{(ls)}$ during sintering, for example, if Ti6Al4V$_{(ls)}$ is introduced to the graphite dies in the horizontal length segment. As a result, the cylindrical Ti6Al4V$_{(ls)}$ was broken. This indicates that the direction of Ti6Al4V$_{(ls)}$ and its geometry must be chosen very carefully.

In general, there are likely to be two reasons for the successful fabrication of EBM printed Ti6Al4V$_{(ls)}$ with a matrix of $BaTiO_{3(nm)}$ without major deformation as usually expected. First, at the beginning of the process, $BaTiO_3$ powder served as a sacrificial material preventing the lattice structure distortion during the uniaxial die compaction [22]. Second, ceramic nanopowder was used, which triggered the start of the densification process of $BaTiO_3$ at a relatively lower temperature and required a lower sintering temperature as described in the previous section [35]. An additional factor is the shape of the Ti6Al4V$_{(ls)}$, as it was not in extremely complex dimensions that could have been destroyed even in the initial sintering stage.

The EDX elemental mapping results show that the presence of oxygen and aluminium elements are homogeneously distributed but only to their corresponding compounds, as shown in Fig. 4d. The mapping of oxygen (element in $BaTiO_3$) and aluminium (element in Ti6Al4V) was considered because of their characteristic peaks, whose positions are different from other characteristic peaks of elements, as shown in the EDX spectrum in Fig. 4e. As a result, the peaks at the same energy level superimpose each other and therefore cannot be separately visualised as clearly as possible with oxygen and aluminium within the investigated spectrum. Consequently, the mapping clearly indicates that oxygen is only present in the matrix of $BaTiO_{3(nm)}$ and aluminium at Ti6Al4V$_{(ls)}$, showing that both materials are bound together but without their large diffusions to each other in a macroscopic scale. This is probably favourable for poling treatment of a ceramic matrix containing a metal lattice structure. These initial results are promising in terms of realising the piezoelectric properties of matrix $BaTiO_{3(nm)}$ in the presence of Ti6Al4V$_{(ls)}$ and mechanical properties of both Ti6Al4V$_{(ls)}$ and $BaTiO_{3(nm)}$ for their potential implantation as a metal-ceramic piezoelectric composite scaffold in load-bearing areas.

4.3. X-ray diffraction

XRD patterns of $BaTiO_{3(nm)}$ and FAST/SPS processed $BaTiO_3$ of Ti6Al4V$_{(ls)}$-$BaTiO_{3(nm)}$ composite were processed by Rietveld refinement [36] and presented in Fig. 5 along with the Bragg positions of the corresponding phase. The mixture of cubic (*C*) and tetragonal (*T*) phases of $BaTiO_3$ are present in both patterns. A minor impurity of $BaCO_3$ can also be found in commercial powder, which is reduced but remains in the FAST/SPS processed sample, as presented in Table 2. This $BaCO_3$ phase does not necessarily prevent its use as a biomaterials [37]. Additionally, it was determined that the crystallite size (*CS*) of both $BaTiO_3$ phases increased to a certain extent but remained within the range of nm (see Table 2) due to the fast sintering process with a relatively lower sintering temperature compared to conventional sintering [18]. This *CS*

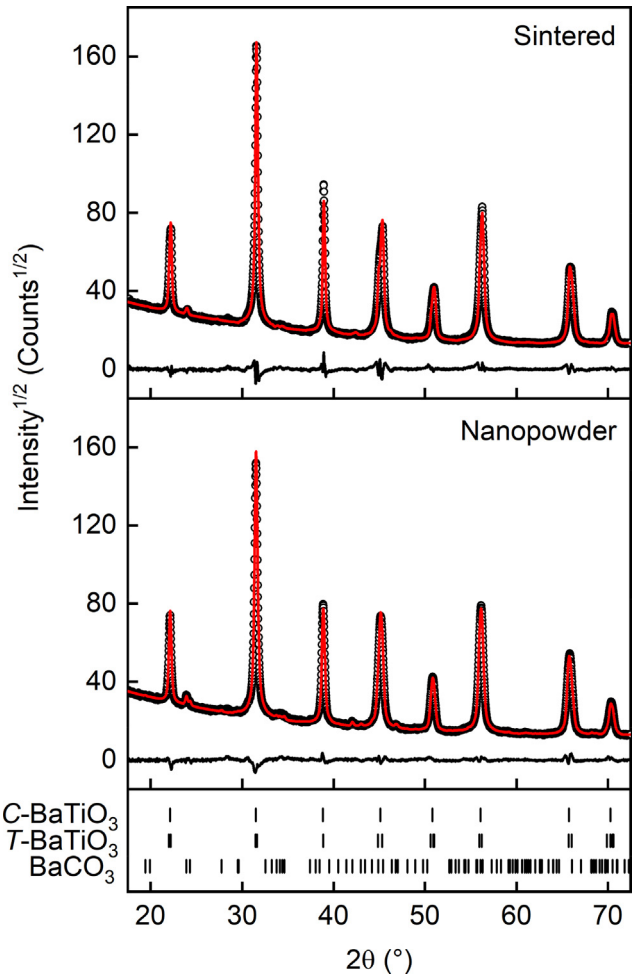

Fig. 5. XRD patterns of the $BaTiO_{3(nm)}$ and the FAST/SPS processed $BaTiO_3$ of Ti6Al4V$_{(ls)}$-$BaTiO_{3(nm)}$ composite. Black dots – experimental pattern and red line – fitted pattern. Below each diffraction pattern the differential patter is presented as a black line. Moreover, corresponding Bragg positions of all contributed phases are shown. (For interpretation of the references to colour in this figure legend, the reader is referred to the web version of this article.)

Table 2
Determined average crystallite sizes (CS) of the $BaTiO_{3(nm)}$ and the FAST/SPS processed $BaTiO_3$ of $Ti6Al4V_{(ls)}$-$BaTiO_{3(nm)}$ composite as well as weight fractions of contributed phases are given.

	CS (nm)		Phases (wt%)		
	C-$BaTiO_3$	T-$BaTiO_3$	C-$BaTiO_3$	T-$BaTiO_3$	$BaCO_3$
Nanopowder	30 ± 7	25 ± 1	58.5 ± 0.5	39.8 ± 0.4	1.7 ± 0.3
FAST/SPS	41 ± 1	31 ± 1	29.6 ± 0.5	69.0 ± 0.1	1.0 ± 0.2

increase can be related to the recrystallisation process during sintering [20]. In addition, the amount of *C*-$BaTiO_3$ phase in weight percent is much higher than the *T*-$BaTiO_3$ phase but becomes lower after the FAST/SPS process by increasing the amount of *T*-$BaTiO_3$ (see Table 2). It indicates that during sintering, a proportion of *C*-$BaTiO_3$ phases transformed to *T*-$BaTiO_3$ which was also observed by Chen et al. when heating $BaTiO_3$ powder to about 1100 °C [38]. This phase transformation from *C*-$BaTiO_3$ to *T*-$BaTiO_3$ favours piezoelectric properties in $BaTiO_3$. Unlike *T*-$BaTiO_3$, *C*-$BaTiO_3$ does not have non-centrosymmetric charge distribution, which is necessary to generate a piezoelectric effect [39,40].

4.4. Corona poling and piezoelectricity

The piezoelectric response of the FAST/SPS processed $Ti6Al4V_{(ls)}$-$BaTiO_{3(nm)}$ composite was determined directly after FAST/SPS. It is noticeable that the composite scaffold exhibited a piezoelectric effect even before corona poling, as presented in Fig. 6. This effect is observed by average d_{33} values on both sides of the scaffold as positive (d_{33+}) and negative (d_{33-}) through the direct piezoelectric response. It indicates that the electric dipoles of $BaTiO_3$ are partially aligned during the FAST/SPS process and the net polarisation of the existing *T*-$BaTiO_3$ phase is non-zero. It is assumed that the applied Direct Current (DC) pulses for the sintering indicate the densification process and act as the source which triggers dipoles to align themselves [18,39]. This may conceivably be done by FAST/SPS electrodes (source of DC pulses) which could have behaved like the poling treatment of sintering material, most probably near the region where current flowed through the material leading to the initial stage of the densification process together with partial dipole alignment [20,41,42]. This effect may also favour the distributed dipoles randomly aligned in the same direction causing remanent polarisation.

The corona poling of FAST/SPS processed $Ti6Al4V_{(ls)}$-$BaTiO_{3(nm)}$ composite gives even more promising results in terms of piezoelectricity in the $Ti6Al4V_{(ls)}$-$BaTiO_{3(nm)}$ composite scaffold. In this direction, the main challenge is the poling of piezoelectric ceramic that contains a substantial amount of bulk conducting metal inside. Electrons can pass through the metal as electrical conduction, which inhibits the alignment of dipoles due to the rapid drop of electric field strength, which is necessary for poling [43]. Nevertheless, the bulk $Ti6Al4V_{(ls)}$-$BaTiO_{3(nm)}$ composite is successfully poled in this work. It was observed that the average piezoelectric constant significantly increased after poling from 0.63 ± 0.12 pC/N to 4.92 ± 0.75 pC/N and −0.41 ± 0.23 pC/N to −4.68 ± 0.56 pC/N in positive and negative electrode sides, respectively. These average piezoelectric values are close to the values of natural bone as well as the synthetic porous piezoelectric $BaTiO_3$ and $BaTiO_3$/Hydroxyapatite composite biomaterials [6,8,44]. It reveals that corona poling of $BaTiO_3$ matrix is possible together with $Ti6Al4V_{(ls)}$ because of contactless poling as there was no direct contact of $Ti6Al4V_{(ls)}$ to the plate electrode due to the insulating $BaTiO_{3(nm)}$ matrix. As a result, electrons did not find a direct path to flow between the electrodes and through the metal $Ti6Al4V_{(ls)}$. Instead, the electric field inside the sample aligns the electric dipoles, resulting in an increased net polarisation. It also supports our previous explanation concerning the partial alignment of dipoles during sintering in the presence of $Ti6Al4V_{(ls)}$. Although the possible effect that can happen is the Faraday cage effect. It could shield the ceramic matrix from the external electric field due to a hollow cylindrical metal scaffold which may suppress electric dipole alignment [45]. This Faraday cage effect was also not decisive, which was most probably due to the cross-sectional direction of $Ti6Al4V_{(ls)}$ to the external electric field (Fig. 2). Since the cylindrical shape $Ti6Al4V_{(ls)}$ is hollow, the electric charges within the composite scaffold have not significantly redistributed and do not cancel the electric field effect. However, the Faraday effect may create a barrier which is most probably between the inner part of the ceramic matrix and the external electric field if the $Ti6Al4V_{(ls)}$ is in the horizontal length segment direction to the electric field. As a result, it may decrease the net polarisation strength. This effect can be even higher with complex Ti6Al4V structures in the composite scaffolds. Nevertheless, further tuning or an increase in piezoelectric constant may also be possible by post sintering-treatment of $Ti6Al4V_{(ls)}$-$BaTiO_{3(nm)}$, i.e. annealing or modifying poling parameters [46,47]. The weight percent of centrosymmetric (*C*-$BaTiO_3$) and non-centrosymmetric (*T*-$BaTiO_3$) phases in sintered scaffold should also be considered to realise the strength of the piezoelectric effect.

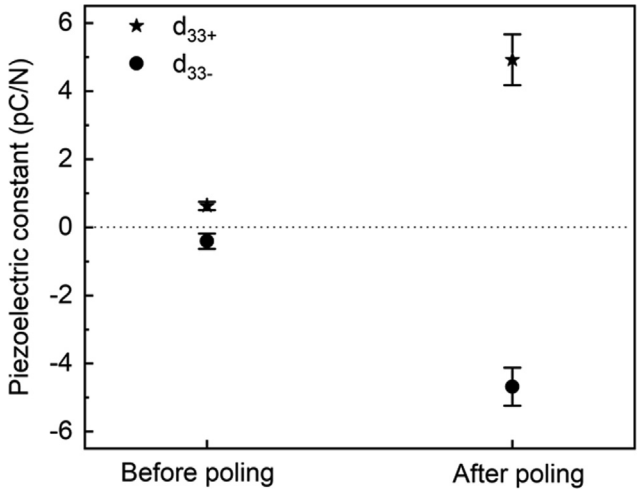

Fig. 6. Average piezoelectric constants of FAST/SPS processed $Ti6Al4V_{(ls)}$-$BaTiO_{3(nm)}$ composite scaffold, both before and after corona poling.

In general, the utilisation of the corona poling setup has two advantages. First, unlike conventional poling treatment, a silicone oil bath, unsuitable for biocompatibility, is not required [48]. Second, no direct electrode contacts are needed, which could promote unfavourable conditions for poling of the $BaTiO_3$ matrix containing $Ti6Al4V_{(ls)}$. Nevertheless, the design and direction of the metal lattice structure and the influence of the Faraday cage effect cannot be ignored. However, in what manner the arrangement of the dipoles and their alignment over the bulk ceramic matrix and close to the metal-ceramic interface appear is still an open question and needs to be considered.

4.5. Nanoindentation

Fig. 7 shows the dependence of the hardness and the Young's modulus of the FAST/SPS processed $Ti6Al4V_{(ls)}$-$BaTiO_{3(nm)}$ composite scaffold on the peak loads. The contact depth of the indenter versus peak load of $Ti6Al4V_{(ls)}$ and $BaTiO_{3(nm)}$ is also presented in supplementary data Figure A1. It can be seen in Fig. 7a that the hardness of $Ti6Al4V_{(ls)}$ is much higher than $BaTiO_{3(nm)}$. It also has a clear dependence on the peak load. The hardness of $Ti6Al4V_{(ls)}$ decreases with an increasing peak load from ~7.3 GPa at 10 mN

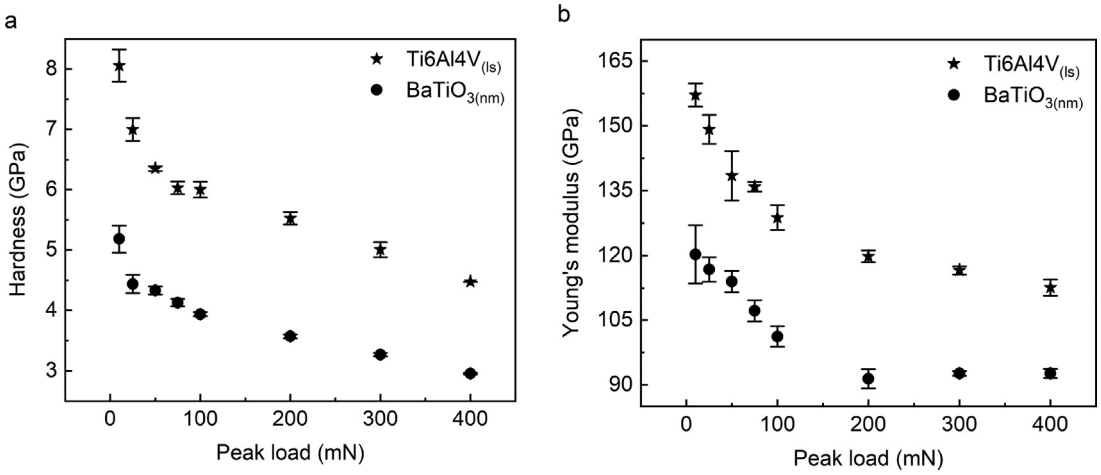

Fig. 7. The dependence of (a) hardness and (b) Young's modulus of the FAST/SPS processed Ti6Al4V$_{(ls)}$-BaTiO$_{3(nm)}$ composite scaffold on the peak loads.

to ~4.5 GPa at 400 mN and the hardness of BaTiO$_{3(nm)}$ decreases with an increasing peak load from ~5.2 GPa at 10 mN to ~3.0 GPa at 400 mN. This dependence may be due to an indentation size effect in the nano-hardness, which has also been raised by several authors [27,49–51]. Likewise, the Young's modulus of Ti6Al4V$_{(ls)}$ is much higher than BaTiO$_{3(nm)}$ as shown in Fig. 7b and dependent on the peak load. The Young's modulus of Ti6Al4V$_{(ls)}$ decreases with an increasing peak load from ~157 GPa at 10 mN to ~113 GPa at 400 mN and the Young's modulus of BaTiO$_{3(nm)}$ decreases with an increasing peak load from ~120 GPa at 10 mN to ~92 GPa at 400 mN. This Young's modulus dependence can be attributed to the indenter tip rounding effect [51]. Nevertheless, the average hardness and Young's modulus of Ti6Al4V$_{(ls)}$ remain higher than BaTiO$_{3(nm)}$ as presented in Table 3. These nanoindentation values show that the Ti6Al4V$_{(ls)}$ is the harder and stiffer part in the Ti6Al4V$_{(ls)}$-BaTiO$_{3(nm)}$ composite scaffold, which can be utilised to enhance the mechanical properties of a scaffold by adding Ti6Al4V$_{(ls)}$ in the matrix of piezoelectric BaTiO$_{3(nm)}$. This hardness and Young's modulus values of the Ti6Al4V$_{(ls)}$-BaTiO$_{3(nm)}$ composite scaffold can be adjusted further by changing the sintering conditions and the design of the Ti6Al4V$_{(ls)}$-core [52–54].

4.6. Load-bearing Ti6Al4V$_{(ls)}$-BaTiO$_{3(nm)}$ piezoelectric scaffolds

In recent years, Fan et al. and Tang et al. have focused on the promising approach of BaTiO$_3$ coating on titanium alloys to make it electroactive [13,15]. The authors have presented that the coating of BaTiO$_3$ on titanium alloys scaffold show the improvement of osteogenesis and osseointegration as well as good cell compatibility. Comparably a new approach has been used in this work to fabricate the Ti6Al4V$_{(ls)}$-BaTiO$_{3(nm)}$ composite bulk scaffolds. This approach can help to fabricate the load-bearing composite scaffold with relatively enhanced and controllable piezoelectric constants due to piezoelectric matrix and the possibility of fine-tuning corona poling. As a result, by combining a load-bearing titanium core with a piezoelectric material in one scaffold, the bone remodelling can be stimulated significantly and could result in an overall improved osseointegration. Additionally, the enhancement of the mechanics of a scaffold by adding the Ti6Al4V$_{(ls)}$ in BaTiO$_{3(nm)}$ piezoelectric matrix through coupling EBM and FAST/SPS opens a new possibility to develop bulk metal-ceramic piezoelectric composite scaffolds for load-bearing areas. The microscopic hardness and Young's modulus values of the Ti6Al4V$_{(ls)}$-BaTiO$_{3(nm)}$ scaffolds fabricated in this work are higher than macroscopic bone values or synthetic porous or dense titanium alloy biomaterials [24–26,55,56]. Therefore, the quasi-static mechanical properties, as well as the fatigue strength of the fabricated composite scaffold need to be investigated further.

Table 3
Determined average hardness and Young's modulus of Ti6Al4V$_{(ls)}$-BaTiO$_{3(nm)}$ composite with standard deviation.

Composite scaffold	Hardness (GPa)	Young's modulus (GPa)
Ti6Al4V$_{(ls)}$	5.9 ± 0.9	130 ± 14
BaTiO$_{3(nm)}$	4.0 ± 0.6	106 ± 10

5. Conclusion

Load-bearing Ti6Al4V$_{(ls)}$-BaTiO$_{3(nm)}$ piezoelectric scaffold is successfully fabricated by coupling EBM and FAST/SPS. The hollow cylindrical scaffold with a hexagonal honeycomb Ti6Al4V$_{(ls)}$ was fabricated by EBM. Subsequently, the fabricated metal together with BaTiO$_{3(nm)}$ were sintered in FAST/SPS. The densification behaviour of the composite scaffold showed that BaTiO$_{3(nm)}$ achieved a relative density of 92.0 ± 0.7 % at the sintering temperature of 950 °C without any major deformation of cylindrical Ti6Al4V$_{(ls)}$. Such relative density of BaTiO$_3$ cannot be achieved if the particle size is in the micrometer range. SEM images also revealed that the cylindrical Ti6Al4V$_{(ls)}$ retained its cylindrical shape after the FAST/SPS process without its major deformation. Moreover, the EBM printed Ti6Al4V$_{(ls)}$ bounded with BaTiO$_{3(nm)}$ without any substantial pores. Whereas no major diffusion of metal elements of Ti6Al4V$_{(ls)}$ was observed in the BaTiO$_3$ matrix through elemental mapping by EDX which is favourable for poling treatment of ceramics matrix containing a metal lattice structure. Additionally, XRD patterns of powder and FAST/SPS processed BaTiO$_{3(nm)}$ showed a mixture of *C*-phase and *T*-phase of biocompatible BaTiO$_3$ which are present in both power and sintered patterns with a minor impurity of BaCO$_3$. This *T*-phase of BaTiO$_3$ is the origin of piezoelectric response in composite scaffold that was observed directly after the FAST/SPS process due to the applied DC pulses for the sintering and could act as the source for triggering dipoles to align themselves. The bulk Ti6Al4V$_{(ls)}$-BaTiO$_{3(nm)}$ composite scaffold was also successfully poled, and corona poling increased the average d_{33} values from 0.63 ± 0.12 pC/N to 4.92 ± 0.75 pC/N and −0.41 ± 0.23 pC/N to −4.68 ± 0.56 pC/N in positive and negative electrode sides, respectively. These average d_{33} values are close to the values of natural bone. Moreover, the nanoindentation values show that the Ti6Al4V$_{(ls)}$ is the harder and stiffer part in the

$Ti6Al4V_{(ls)}$-$BaTiO_{3(nm)}$ composite scaffold. The $Ti6Al4V_{(ls)}$ exhibited an average hardness of 5.9 ± 0.9 GPa and Young's modulus of 130 ± 14 GPa. While $BaTiO_{3(nm)}$ had an average hardness of 4.0 ± 0.6 GPa and Young's modulus of 106 ± 10 GPa. It reveals that the mechanical properties of a scaffold can be enhanced by adding $Ti6Al4V_{(ls)}$ in the matrix of piezoelectric $BaTiO_{3(nm)}$. Therefore, the concept of the fabrication of such composite scaffolds by coupling EBM and FAST/SPS opens new possibilities for developing bulk metal-ceramic piezoelectric composite scaffolds for load-bearing areas. The investigation on the tunning of these scaffolds by implementing porosity in $BaTiO_{3(nm)}$ ceramics and the topology of the $Ti6Al4V_{(ls)}$ scaffold to alter the biomechanical and piezoelectric properties as well as the cell-material interaction will be considered in future.

Data availability

The raw data required to reproduce the findings of this published article are available from the corresponding author upon reasonable request.

Data availability

Data will be made available on request.

Declaration of Competing Interest

The authors declare that they have no known competing financial interests or personal relationships that could have appeared to influence the work reported in this paper.

Acknowledgements

This research was funded by the Deutsche Forschungsgemeinschaft (DFG, German Research Foundation) - SFB 1270/2 – 299150580. The authors thank Mr. Benjamin Eichler for the polishing of samples. Miss Caroline Scheufler is also acknowledged for corona poling piezoelectric measurements of the samples.

Appendix A. Supplementary material

Supplementary data to this article can be found online at https://doi.org/10.1016/j.matdes.2022.111428.

References

[1] G.A. Rodan, Introduction to bone biology, Bone 13 (1992) S3–S6.
[2] J.J. Li, M. Ebied, J. Xu, H. Zreiqat, Current approaches to bone tissue engineering: the interface between biology and engineering, Adv. Healthc. Mater. 7 (6) (2018) 1701061.
[3] R. Zhao, R. Yang, P.R. Cooper, Z. Khurshid, A. Shavandi, J. Ratnayake, Bone grafts and substitutes in dentistry: A review of current trends and developments, Molecules 26 (10) (2021) 3007.
[4] B.M. Holzapfel et al., How smart do biomaterials need to be? A translational science and clinical point of view, Adv. Drug Deliv. Rev. 65 (4) (2013) 581–603.
[5] A.H. Rajabi, M. Jaffe, T.L. Arinzeh, Piezoelectric materials for tissue regeneration: A review, Acta Biomater. 24 (2015) 12–23.
[6] B. Tandon, J.J. Blaker, S.H. Cartmell, Piezoelectric materials as stimulatory biomedical materials and scaffolds for bone repair, Acta Biomater. 73 (2018) 1–20.
[7] D. Khare, B. Basu, A.K. Dubey, Electrical stimulation and piezoelectric biomaterials for bone tissue engineering applications, Biomaterials 258 (2020) 120280.
[8] C. Polley et al., 3D Printing of Piezoelectric Barium Titanate-Hydroxyapatite Scaffolds with Interconnected Porosity for Bone Tissue Engineering, Materials 13 (7) (2020) 1773.
[9] K. Zhang et al., Advanced smart biomaterials and constructs for hard tissue engineering and regeneration, Bone Res. 6 (1) (2018) 1–15.
[10] S. Jiang, M. Wang, J. He, A review of biomimetic scaffolds for bone regeneration: Toward a cell-free strategy, Bioeng. Transl. Med. 6 (2) (2021) e10206.
[11] R. Sobreiro-Almeida et al., Human mesenchymal stem cells growth and osteogenic differentiation on piezoelectric poly (vinylidene fluoride) microsphere substrates, Int. J. Mol. Sci. 18 (11) (2017) 2391.
[12] J. George, Y. Kuboki, T. Miyata, Differentiation of mesenchymal stem cells into osteoblasts on honeycomb collagen scaffolds, Biotechnol. Bioeng. 95 (3) (2006) 404–411.
[13] B. Fan et al., Electroactive barium titanate coated titanium scaffold improves osteogenesis and osseointegration with low-intensity pulsed ultrasound for large segmental bone defects, Bioact. Mater. 5 (4) (2020) 1087–1101.
[14] W. Liu et al., Biological effects of a three-dimensionally printed Ti6Al4V scaffold coated with piezoelectric BaTiO3 nanoparticles on bone formation, ACS Appl. Mater. Interfaces 12 (46) (2020) 51885–51903.
[15] Y. Tang, C. Wu, P. Tian, K. Zhao, Z. Wu, Fabrication and induced mineralization of bio-piezoelectric ceramic coating on titanium alloys, Ceram. Int. 46 (3) (2020) 4006–4014.
[16] J. Parthasarathy, B. Starly, S. Raman, A. Christensen, Mechanical evaluation of porous titanium (Ti6Al4V) structures with electron beam melting (EBM), J. Mech. Behav. Biomed. Mater. 3 (3) (2010) 249–259.
[17] A.H. Chern et al., A review on the fatigue behavior of Ti-6Al-4V fabricated by electron beam melting additive manufacturing, Int. J. Fatigue 119 (2019) 173–184.
[18] A. Riaz et al., Structural changes and pseudo-piezoelectric behaviour of field assisted sintered calcium titanate, Materialia 15 (2021) 100998.
[19] C. Shuai et al., Functionalized BaTiO3 enhances piezoelectric effect towards cell response of bone scaffold, Colloids Surf. B Biointerfaces 185 (2020) 110587.
[20] O. Guillon et al., Field-assisted sintering technology/spark plasma sintering: mechanisms, materials, and technology developments, Adv. Eng. Mater. 16 (7) (2014) 830–849.
[21] A. Nisar, C. Zhang, B. Boesl, A. Agarwal, Unconventional materials processing using spark plasma sintering, Ceramics 4 (1) (2021) 20–39.
[22] C. Manière, L. Durand, A. Weibel, G. Chevallier, C. Estournès, A sacrificial material approach for spark plasma sintering of complex shapes, Scr. Mater. 124 (2016) 126–128.
[23] C. Manière, E. Torresani, E.A. Olevsky, Simultaneous spark plasma sintering of multiple complex shapes, Materials 12 (4) (2019) 557.
[24] E. Yılmaz, A. Gökçe, F. Findik, H.O. Gulsoy, O. İyibilgin, Mechanical properties and electrochemical behavior of porous Ti-Nb biomaterials, J. Mech. Behav. Biomed. Mater. 87 (2018) 59–67.
[25] E. Yılmaz, A. Gökçe, F. Findik, H. Gulsoy, Metallurgical properties and biomimetic HA deposition performance of Ti-Nb PIM alloys, J. Alloy. Compd. 746 (2018) 301–313.
[26] N. Aslan, B. Aksakal, F. Findik, Fabrication of porous-Ti6Al4V alloy by using hot pressing technique and Mg space holder for hard-tissue biomedical applications, J. Mater. Sci. - Mater. Med. 32 (7) (2021) 1–11.
[27] W.C. Oliver, G.M. Pharr, An improved technique for determining hardness and elastic modulus using load and displacement sensing indentation experiments, J. Mater. Res. 7 (6) (1992) 1564–1583.
[28] Y. Nakagawa, H. Yoshida, A. Uehashi, T. Tokunaga, K. Sasaki, T. Yamamoto, Electric current-controlled synthesis of BaTiO3, J. Am. Ceram. Soc. 100 (9) (2017) 3843–3850.
[29] A. Uehashi, H. Yoshida, T. Tokunaga, K. Sasaki, T. Yamamoto, Enhancement of sintering rates in BaTiO3 by controlling of DC electric current, J. Ceram. Soc. Jpn. 123 (1438) (2015) 465–468.
[30] Y. F. Yang, M. Qian, "Spark plasma sintering and hot pressing of titanium and titanium alloys," in Titanium powder metallurgy: Elsevier, 2015, pp. 219-235.
[31] D. Garbiec, P. Siwak, A. Mróz, Effect of compaction pressure and heating rate on microstructure and mechanical properties of spark plasma sintered Ti6Al4V alloy, Arch. Civil Mech. Eng. 16 (4) (2016) 702–707.
[32] X. Yang et al., Colossal dielectric performance of pure barium titanate ceramics consolidated by spark plasma sintering, RSC Adv. 6 (79) (2016) 75422–75429.
[33] R. Rahmani, M. Antonov, L. Kollo, Y. Holovenko, K.G. Prashanth, Mechanical behavior of Ti6Al4V scaffolds filled with CaSiO3 for implant applications, Appl. Sci. 9 (18) (2019) 3844.
[34] R. Rahmani, M. Rosenberg, A. Ivask, L. Kollo, Comparison of Mechanical and Antibacterial Properties of TiO2/Ag Ceramics and Ti6Al4V-TiO2/Ag Composite Materials Using Combined SLM-SPS Techniques, Metals 9 (8) (2019) 874.
[35] D.V. Dudina, B.B. Bokhonov, E.A. Olevsky, Fabrication of porous materials by spark plasma sintering: a review, Materials 12 (3) (2019) 541.
[36] R. E. Dinnebier, A. Leineweber, J. S. Evans, "Rietveld refinement," in Rietveld Refinement: de Gruyter, 2018.
[37] M. Raessi et al., Barium carbonate nanostructures: Biosynthesis and their biomedical applications, Ceram. Int. 47 (15) (2021) 21045–21050.
[38] C. Chen et al., Nano-BaTiO3 phase transition behavior in coated BaTiO3-based dielectric ceramics, Ceram. Int. 45 (6) (2019) 7166–7172.
[39] A. Riaz et al., Tunable Pseudo-Piezoelectric Effect in Doped Calcium Titanate for Bone Tissue Engineering, Materials 14 (6) (2021) 1495.
[40] D.-S. Park et al., Induced giant piezoelectricity in centrosymmetric oxides, Science 375 (6581) (2022) 653–657.
[41] M. Bram et al., Application of electric current-assisted sintering techniques for the processing of advanced materials, Adv. Eng. Mater. 22 (6) (2020) 2000051.
[42] M. Biesuz, D. Rizzi, V.M. Sglavo, Electric current effect during the early stages of field-assisted sintering, J. Am. Ceram. Soc. 102 (2) (2019) 813–822.
[43] S. Kasap, C. Koughia, H. E. Ruda, "Electrical conduction in metals and semiconductors," in Springer handbook of electronic and photonic materials: Springer, 2017, pp. 1-1.

[44] Y. Zhang, L. Chen, J. Zeng, K. Zhou, D. Zhang, Aligned porous barium titanate/hydroxyapatite composites with high piezoelectric coefficients for bone tissue engineering, Mater. Sci. Eng. C 39 (2014) 143–149.
[45] Y. Hwang, Y. Je, D. Farrar, J.E. West, S.M. Yu, W. Moon, Piezoelectric properties of polypeptide-PMMA molecular composites fabricated by contact charging, Polymer 52 (13) (2011) 2723–2728.
[46] G.P. Khanal, S. Kim, M. Kim, I. Fujii, S. Ueno, S. Wada, Grain-size dependence of piezoelectric properties in thermally annealed BaTiO3 ceramics, J. Ceram. Soc. Jpn. 126 (7) (2018) 536–541.
[47] G.P. Khanal et al., Effect of thermal annealing on crystal structures and electrical properties in BaTiO3 ceramics, J. Appl. Phys. 124 (3) (2018) 034102.
[48] C. Yang, K. Chen, W.-M. Hsu, Y. Li, Cytotoxicity of silicone oil on cultivated human corneal endothelium, Eye 22 (2) (2008) 282–288.
[49] W.C. Oliver, G.M. Pharr, Measurement of hardness and elastic modulus by instrumented indentation: Advances in understanding and refinements to methodology, J. Mater. Res. 19 (1) (2004) 3–20.
[50] G. Zhang, Z. Wei, R.E. Ferrell, Elastic modulus and hardness of muscovite and rectorite determined by nanoindentation, Appl. Clay Sci. 43 (2) (2009) 271–281.
[51] J. Gong, H. Miao, Z. Peng, L. Qi, Effect of peak load on the determination of hardness and Young's modulus of hot-pressed Si3N4 by nanoindentation, Mater. Sci. Eng. A 354 (1–2) (2003) 140–145.
[52] O.E. Falodun, B.A. Obadele, S.R. Oke, A.M. Okoro, P.A. Olubambi, Titanium-based matrix composites reinforced with particulate, microstructure, and mechanical properties using spark plasma sintering technique: a review, Int. J. Adv. Manuf. Technol. 102 (5) (2019) 1689–1701.
[53] S.D. Oguntuyi, O.T. Johnson, M.B. Shongwe, Spark plasma sintering of ceramic matrix composite of TiC: microstructure, densification, and mechanical properties: a review, Int. J. Adv. Manuf. Technol. 116 (1) (2021) 69–82.
[54] A.M. Okoro, S.S. Lephuthing, S.R. Oke, O.E. Falodun, M.A. Awotunde, P.A. Olubambi, A review of spark plasma sintering of carbon nanotubes reinforced titanium-based nanocomposites: fabrication, densification, and mechanical properties, JOM 71 (2) (2019) 567–584.
[55] J. Black and G. Hastings, Handbook of biomaterial properties. Springer Science & Business Media, 2013.
[56] J.L. Katz, Anisotropy of Young's modulus of bone, Nature 283 (5742) (1980) 106–107.